

Cloud water-phase dynamics observed by microwave profiling radiometry and vertically-pointing radar

Edwin F. Campos^{1*}, Randolph Ware^{2,3}, Paul Joe¹, and David Hudak¹

¹*Cloud Physics and Severe Weather Research Section, Environment Canada, Toronto, Ontario, Canada.*

²*Radiometrics Corporation, Boulder, Colorado, USA*

³*Mesoscale and Microscale Meteorology Division, National Center for Atmospheric Research, Boulder, Colorado, USA*

To be submitted to the Journal of Oceanic and Atmospheric Technology

12 January 2010

Abstract

Dynamic exchange among water solid, liquid and vapor phases determines the evolution of cloud and precipitation particles in the atmosphere. This work presents observations of water phase dynamics that demonstrates the theoretical Wegener-Bergeron-Findeisen concepts in mixed-phase winter-cloud systems. For this, the work analyzes vertical profiles of temperature, relative humidity, vapor density, and cloud liquid-water content. All profiles were simultaneously retrieved during two snow storms, using two distinct microwave profiling radiometers operating in different climatic regions (North American Central High Plains and Great Lakes). To corroborate our analyses, we use reflectivity factor and Doppler velocity observations by vertically-pointing radars located near the radiometers. Based only on the magnitude ranking of in-cloud vapor pressures and equilibrium vapor pressures over liquid water and over ice, we identified conditions where liquid droplets and ice particles grow or deplete simultaneously, as well as the conditions where droplets evaporate and ice particles grow by vapor diffusion.

1. Introduction

Nowcasting of mixed-phase precipitation is important because it is often associated to adverse weather. Icing conditions and reduced visibility on airport runways, roads, or aircrafts, represent a hazard for ground and air transportation. Adverse icing and visibility conditions also compromise competition fairness during high-profile sport events such as the winter Olympics. Glaciated, liquid and vapor water phases often co-exist within each North-American winter storm. Aircraft measurement analysis by Cober et al. (2001, p.1992) found that, at temperatures from 0° to -20°C, approximately 40% of the time there are mixed-phase cloud particles.

Water budget exchanges among solid, liquid and vapor phases describe the evolution of cloud and precipitation particles in the atmosphere. Observing these water exchanges among natural snow and cloud droplets is very challenging, because it requires simultaneous monitoring of very distinct variables, sampled at cloud scales and at intervals of only few minutes. Laboratory observations, usually involving complex experiments in controlled environments, are a way to build conceptual hypotheses about water phase exchanges in clouds. In natural clouds, however, observations by radiosonde, instrumented-aircraft, or radar are insufficient to provide robust validation to these conceptual hypotheses. Radiosonde and aircraft instruments provide observations only during a very limited number of vertical profiles, and radar observations are not sensitive to water-vapor targets.

Consider a cloud consisting of water vapor, liquid droplets, and ice particles. The rate of condensational growth (or evaporation) of the droplets and ice particles in this mixed-phase cloud is proportional to the difference between in-cloud vapor pressure (e) and equilibrium vapor pressure over liquid water (e_s) and ice (e_i), respectively. Since at subfreezing temperatures $e_s > e_i$, there are three possible inequalities among e , e_s , and e_i (Korolev 2007), thereby resulting in three scenarios for the evolution of mixed-phase clouds:

Scenario 1: Droplet-ice growth, $e > e_s > e_i$. In this case, droplets and ice particles grow simultaneously by vapor diffusion. The liquid droplets and ice particles both compete for water vapor. This condition may occur in ascending mixed-phase clouds. This may also occur in zones of isobaric mixing.

Scenario 2: Evaporation deposition, $e_s > e > e_i$. In this case, droplets evaporate, whereas ice particles grow by vapor diffusion (deposition). This is the most widely-known of the three, and is often called the Wegener-Bergeron-Findeisen process. In mixed-phase clouds, this may occur in both updrafts and downdrafts.

Scenario 3: Droplet-ice depletion, $e_s > e_i > e$. In this case, droplets and ice particles deplete simultaneously. Droplet evaporation and ice-particle sublimation may occur due to entrainment and mixing with environmental dry air near the cloud boundaries.

The following sections will present, for the first time, observations from Microwave Profiling Radiometer that validate the occurrence of these theoretical scenarios in natural clouds. This paper also demonstrates that water exchanges in mixed-phase clouds can be observed by using measurements from a Microwave Profiling Radiometer. For that, the article presents analyses and interpretation of observations during snowstorms taken by two similar radiometers placed at different climate locations.

2. Methods

a. Experimental setup

Two snowstorm examples are presented, the first corresponds to a winter lake-effect event, occurring on 23 February 2006 at Environment Canada Centre for Atmospheric Research Experiments (CARE, located about 80 km N of Toronto, in Ontario, Canada). For this event, precipitation was observed at ground level in the form of melting snow, starting around 16 UTC and finishing by 2230 UTC. For these analyses, a 12-channel measurements from a microwave profiling radiometer was used (Radiometrics model TP/WVP-3000). It was located at 44.23°N, 79.78°W, and 249 m above sea level. In addition, a X-band vertically-pointing radar provided co-located complementary observations of this snowstorm.

The second example is a winter upslope snowstorm, occurring on 14 February 2008 at Boulder (Colorado, USA). For this event, precipitation was observed at the ground in the form of powder (very dense and small particles) snow, for a period roughly between 08 and 18 UTC. For these analyses, a 22-channel measurements from a microwave profiling radiometer was used (Radiometrics model MP-3000A). It was located at 40.01°N, 105.15°W, and 1616 m above the sea level. In addition, an UHF-band vertically-pointing radar provided co-located complementary observations of this snowstorm.

b. Radiometer sensors

The radiometer observes atmospheric microwave and infrared emission along with surface temperature, humidity and pressure. Every minute, it converts these observations into vertical profiles of air temperature, of relative humidity, of water vapor content (density), and of cloud liquid-water content (density). Each profile is retrieved independently using a neural network algorithm (Solheim et al. 1998) trained by forward modeling many years of historical operational radiosonde data with a radiative transfer model (Rosenkranz 1998). The vertical resolution of the

retrieved profiles is 100 m from 0-2 km height for the TP/WVP-3000, 50 m for 0-0.5 km height and 100m for 0.5-2 km for the MP-3000A, and 250 m from 2-10 km height for both instruments.

To guarantee the highest accuracy in radiometer retrievals, the 22-30 GHz receiver (a noise diode) was calibrated before taking all measurements in this work. For this, the radiometer used the precipitation-free atmosphere as a cold target. By observing the brightness temperature of the sky at several elevation angles in rapid succession, the profiling radiometer then computed an estimate of the 22-30 GHz noise-diode temperatures. Details on this calibration method are presented by Radiometrics (2007, p.41). Similarly, the 51-59 GHz receiver was calibrated beforehand, using a external liquid nitrogen target (brightness temperature near 78 K) and an internal ambient target (brightness temperature near 278 K), according to the method presented by Radiometrics (2007, p.33).

Liquid water on a radiometer radome can result in artificially high values of brightness temperature. However, the profiling radiometers used in this study have radomes made with hydrophobic materials, in addition to a blower that minimizes accumulation of liquid water on the radome surface. Furthermore, next to the radiometer radome, there is a sensor board measuring conductivity across a grid of gold-plated conductors. This sensor board provides a flag for data that is potentially contaminated by liquid water on the radome. The data in this paper have been filtered using this precipitation flag.

Statistical comparisons with simultaneous radiosonde observations (Güldner and Spänkuch 2001; Liljegen et al. 2001; Cimini et al. 2006a and 2006b), demonstrate that the difference in temperature and vapor density values are smaller than 1°C and smaller than 1 g m⁻³, respectively, for heights below 500 m, over all seasons and at various locations. These differences are smaller than the representativeness error inherent in (radiosonde) point measurements below 500 m height, and are comparable above 500 m height (Ware et al. 2003, Knupp et al. 2008). The radiometer accuracy and high temporal resolution, coupled with its water-vapor and liquid-water profiling capabilities, make it ideal to study water phase changes inherent in precipitation storms.

Absolute errors in radiometer liquid-water retrievals are difficult to quantify, since radiosondes do not measure liquid water, and in situ validation should depend on scarcer aircraft observations. Korolev et al. (2007, Fig. 8) present radiometer bias for liquid-water paths in the order of 100 g m⁻², obtained by comparing a 2-channel radiometer (37 and 85 GHz, Koldaev et al. 1999) with in situ (aircraft) observations. We expect our absolute errors to be much smaller than 100 g m⁻², considering that the radiometers used in our work use 12- and 22-channel receivers, with more modern (at least by a decade) hardware and software.

Radiometer retrieval errors in liquid water estimates can be due to errors in the coefficients output by the neural-network algorithm (mainly random errors) and errors in the brightness temperature measurements (mainly systematic errors). We have minimized the systematic errors by careful and constant calibration of the radiometer receivers (as explained previously). Standard errors in the neural network retrievals of cloud liquid water contents are, in our experience, in the order of 0.01 g m⁻³. Thus, liquid water contents smaller than 0.02 g m⁻³ will be considered as retrieval noise here. (Notice that retrieved values smaller than this threshold can occur during clear skies.)

The radiometer retrievals of temperature and vapor density are used for computing e , e_s , and e_i , which are then used to determine if observed water phase changes agree with theoretical scenarios. Vapor pressure (e) calculations use Rogers and Yau (1991, p.12). The computations for equilibrium vapor pressure over liquid water (e_s) and over ice (e_i) follows Pruppacher and Klett (1997, p.854).

c. Radar sensors

Vertically-pointing Doppler radars, co-located with the radiometers, provided complementary observations for this study, which allowed qualitative validation of the radiometer retrievals. The McGill Vertically Pointing Doppler Radar (VPRD) was used for the winter lake-effect event (on 23 February 2006). This is a X-band (9.35 GHz) radar, operated by McGill University, and it is described by Zawadzki et al. (2001). By comparison with co-located ground sensors, we estimate that this radar was able to detect snow at lower heights only for intensities greater than about 0.02 mm h^{-1} .

The NCAR-ISS wind profiler was used for the winter upslope event (on 14 February 2008). This is a vertically-pointing Doppler radar, operated by NCAR Foothills Laboratory, and is located 1 km north of the radiometer site. This UHF-band (915 MHz) radar wind profiler, is described by Parsons et al. (1994, and references therein). This radar was calibrated to provide radar reflectivity factors with accuracies in the order of 5 dB (W. Brown, 2008, personal communication).

Further details on these radars are given in Table 1.

3. Results

a. Lake-effect snowstorm

Lake-effect snowstorms are winter weather patterns common along the lee shores of the North American Great Lakes. Extensive literature is available on the climatological and synoptic contexts where these storms evolve (e.g., Liu and Moore 2004, and references therein). Concentrating here on the cloud-scale context, Figure 1 presents radiometer observations of a winter lake-effect snowstorm, on 23 Feb 2006 at the CARE site (Ontario, Canada). The first three panels from top to bottom correspond to retrieved vertical profiles of air temperature, vapor density, and cloud liquid-water content. The temperature plot (panel A) shows a horizontally stratified thermal pattern, which is characteristic of lake-effect snowstorms (cold-air masses transport flow over the warmer surface of a North American Great Lake, resulting in cloud formation and large snowfall amounts to the lee side of the lakes). Note also that the zero Celsius isoline is above the ground level between 16 and 22 UTC, therefore producing melting snow at ground level. In panel B, observe the period of increase in vapor density between 13 and 19 UTC, and the period of decrease in vapor density between 19 and 23 UTC. This last period of water vapor depletion is matched by the presence of liquid water at heights roughly between 1 and 2 km (see panel C in Fig.1). This liquid water is supercooled, because it is present in regions of the atmosphere where the temperature is below freezing (see top panel in Fig.1). The following question arises: Is this supercooled liquid water (detected between 19 and 23 UTC, 23 Feb 2006) responsible for the observed depletion in water vapor density?

To address this question, the bottom panel in Fig.1 provides a vapor-pressure classification for the entire event. In this bottom panel, the green regions correspond to the droplet-ice growth scenario, the yellow indicate regions where the evaporation deposition scenario occurs, and the red corresponds to the droplet-ice depletion scenario. Melting snow was observed at ground between 16 and 22 UTC. Solid and liquid water phases were growing between 19 and 22 UTC. If droplet-ice growth conditions exist then the source of the growth must be the supercooled liquid water. In Fig.1.D, the droplet-ice growth scenario is observed between 19 and 22 UTC, at heights above 1km and below 3.5 km, roughly. Supercooled water was observed between 22 and 23 UTC (panel C in Fig.1), and it also occurred when droplet-ice growth conditions apply (panel D in Fig.1).

A more detailed analysis is possible by identifying the vertical distribution of precipitation particles. Figure 2 presents observations by the X-band vertically-pointing radar during the same snowstorm. The upper panel corresponds to radar reflectivity factor (in dBZ), and the lower panel

corresponds to vertical Doppler velocity (in m s^{-1}). Precipitation features are evident here for the snow storm discussed in the previous two paragraphs. For the precipitation patch between 07 and 12 UTC, at heights between 3 and 6 km, the lower panel indicates that these are snow or drizzle particles, because Doppler fall velocities are between zero and 2 m s^{-1} . According to the radiometer observations, this corresponds to an increase in vapor density (panel B in Fig.1). However, the vapor pressure conditions indicate evaporation and sublimation for heights below 4 km (droplet-ice depletion conditions in lower panel of Fig.1). The radar observations are consistent with the radiometer estimates.

It is interesting that cloud liquid-water contents in the range $0.02\text{-}0.06 \text{ g m}^{-3}$ are detected by the radiometer between 0730 and 1230 UTC, at levels from 1.5 to 3.5 km height (panel C in Fig.1), and that the radar detects precipitation particles from 3 to 6 km height during this time period (Fig.2). However, this is occurring in a region corresponding to conditions of droplet-ice depletion (lower panel in Fig.1). This apparent contradiction (of observing precipitation in a region of particle depletion) is clarified by realizing that the radar detects precipitation particles during this time period, while the radiometer detects cloud droplets. As the size of the precipitation particles reduces by vapor diffusion, there is a point where all or part of the liquid particles reach droplet sizes. The X-band radar cannot detect these cloud droplets, but the radiometer is able to detect cloud liquid water at this point. There is also the possibility of particles that originally evolved in a region with different conditions than those observed at the zenith, and that are transported (advected) later into the radiometer sampling volume. In any case, the combination of radar and radiometer measurements provides again a unique insight into the three theoretical cases discussed in the Introduction.

b. Winter upslope snowstorm

Climatology and dynamics of winter upslope snowstorms, along the eastern margin of the Colorado Rockies, are well understood at the synoptic scale (e.g., Dunn 1987, Mahoney et al. 1995). Concentrating here on the cloud scale, Fig.3 shows radiometer observations for the onset and development of a winter upslope snowstorm, on 14 February 2008 at Boulder. Panels in this figure, from top to bottom, correspond to vertical profiles of air temperature, vapor density, cloud liquid-water content, and vapor-pressure class. The periods after 0836 UTC (in all panels) are filled with white lines to indicate the presence of liquid water on the radiometer radome (mainly from melting snow). A cold front arrived at the radiometer site around 0415 UTC (panel A). The retrieved profiles show the sharp drop in temperature and rise in vapor density (panel B in Fig.3) that occurred below 3 km height. Then the vapor density (panel B in Fig.3) starts to decrease when cloud liquid-water content increases (at about 06 UTC, panel C in Fig.3). From panels A and C in Fig.3, the cloud liquid water is supercooled (between 0° and -13°C). Condensation of supercooled liquid appears to deplete the water vapor density. The period between 06 and 09 UTC corresponds to droplet-ice growth (panel D in Fig.3). However, the following questions arise: (1) Why is cloud liquid water not observed in the period between 0430 and 06 UTC (i.e., right after the front passes over the radiometer site)? and (2) What makes the cloud liquid water disappear after 09 UTC?

The period between 0430 and 06 UTC, as well as the one after 09 UTC, have regions of droplet-ice growth, but radiometer observations do not indicate cloud liquid-water in these periods. The first period (between 0430 and 06 UTC) most likely corresponds to conditions where haze droplets are growing towards cloud-droplet sizes (i.e., when droplets condensation nuclei become activated and its growth does not longer need an increasing supersaturation; Rogers and Yau 1991, p.89). Recall that for a haze particle to grow into a cloud particle, it is not sufficient to have $e > e_s$, but rather to have reached a critical radius within a critical equilibrium

supersaturation. Haze critical radii are in the order of $1 \mu\text{m}$, and the equilibrium supersaturations $[(e/e_s) - 1]$ are in the order of 10^{-3} or smaller (Pruppacher and Klett 1997, p.176). With these considerations, and based on haze droplet-size distributions measured at ground (Gultepe et al. 2008, Fig.12, green curve for diameters of $1.7 \mu\text{m}$ or less), we estimate that haze liquid-water contents are in the order of $7 \times 10^{-5} \text{ g m}^{-3}$. This magnitude is much smaller than the radiometer retrieval error (10^{-2} g m^{-3} , as in section 2.b). Therefore, liquid water contents from haze cannot be retrieved by the radiometer. For the observations on 14 Feb 2008, it is only after 06 UTC that the droplets are large enough (in number and size) to be retrieved by the radiometer (in panel C, Fig 3). The positive outcome is that our analysis of vapor-pressure classes (panels D in Figs. 1 and 3) are providing more than one-hour lead time in the forecasting of supercooled liquid water. In other words, the droplet-ice growth scenario appears much earlier than the 0.02 g m^{-3} LWC contours.

A more detailed analysis of the entire event is possible by analyzing co-located observations from vertically-pointing radar. Fig. 4 presents observations by a UHF-band wind profiler during the same snowstorm. The upper panel corresponds to radar reflectivity factor (in dBZ), and the lower panel corresponds to vertical Doppler velocity (in m s^{-1}). The period before 07 UTC is characterized by updrafts (negative Doppler velocities in lower panel, Fig.4). This ascending air is responsible for transporting new amounts of water vapor aloft. The radar signals detected during this period are actually from clear-air targets (i.e., from sharp discontinuities in the index of refraction, an index that depends on air temperature, vapor pressure and air pressure; e.g., Rottger and Larsen 1990). These targets can be detected at UHF band but not at X band. For example, the sharp spatial gradients of temperature and vapor pressure retrieved by the radiometer at 0415 UTC in Fig.3 (due to the frontal passage over the radiometer site) are matched by sharp UHF reflectivity values right after 0415 UTC (Fig.4).

To answer the second question, of why the observed liquid water disappeared after 9 UTC, notice in Fig.4 the radar echoes with reflectivity factors larger than 10 dBZ. The associated Doppler vertical velocities are smaller than 2 m s^{-1} downwards. These echoes reach above 2 km height only after about 0830 UTC. These are evidence of dense snow, which was also observed at ground level as dense tiny snow particles. Consistent with the ice and snow growth by vapor deposition, the liquid water depletes, beginning around 0830 UTC. All liquid water is eliminated by 0930 UTC (panel C, Fig.3). In addition, continuing depletion of water vapor near 1km height (panel B, Fig.3) is consistent with snow vapor deposition. Furthermore, Doppler vertical velocities below 1.5 km height (after 0830 UTC) are larger than 3 m s^{-1} , which is a typical value for riming snow or small raindrops (diameters around 0.8 mm; e.g., Gunn and Kinzer 1949). All these suggest that, for the period following 0830 UTC, supercooled droplets are being captured by snow particles during riming, right from its first formation at levels above the 2 km. Therefore, the radiometer observations indicate a dramatic reduction in cloud liquid-water content until it is completely depleted by 09 UTC (panel C, Fig.3). Finally, an evaporation-deposition region appears approximately after 0840 UTC, for heights above 3.2 km (panel C in Fig.3). This implies that $e_s > e$ at the heights where droplets previously were starting to form, and any droplets existing there must evaporate after that time. Since droplets formation conditions vanish aloft, and riming conditions appear above 2 km height, the droplets will deplete along the vertical column after about 09 UTC.

4. Conclusions

This contribution presents examples of remote-sensing observations (using radiometry and radar) of water exchanges among the solid, liquid, and gas phases, in conditions including natural clouds. The analyses focus on two snowstorms from two different climatic regions in North

America, the Great Lakes and the Central High Plains. They verify theoretical concepts postulated by Wegener (1911), Bergeron (1935) and Findeisen (1935), and summarized by Korolev (2007).

Based only on the magnitude ranking of in-cloud vapor pressures and equilibrium vapor pressures over liquid water and over ice, this work identified conditions where liquid droplets and ice particles grow or deplete simultaneously, as well as the conditions where droplets evaporate and ice particles grow by deposition from vapor diffusion.

This study showed how radiometer profiling provides new insights to complex relationships between temperature, relative humidity, cloud liquid and ice contents, and vapor density during snow storms. Monitoring these thermodynamic variables allow the identification of winter-storm regions with growth or depletion of ice particles and droplets.

Accretion and coalescence are other scenarios, in addition to the three discussed in the Introduction, by which droplets can be depleted (Rogers and Yau 1991, p.163). Recall the last paragraph of Section 5, which noted in Fig.3 (after 0830 UTC and above 2 km height) that supercooled droplets were captured by snow particles during riming (i.e., accretion followed by freezing). The three scenarios discussed in the Introduction (droplet-ice growth, evaporation deposition and droplet-ice depletion) are most important during the earlier stages of cloud formation, while accretion and coalescence are most important during the mature stages of a precipitating cloud. Since radiometer retrievals are optimized for conditions without liquid precipitation, the analysis technique presented here (for identifying water-phase dynamics) should then perform better during the early stages of cloud formation (rather than during the mature precipitating-cloud stages).

The results of radiometer data analyses were enhanced significantly when combined with complementary vertically-pointing radar data. Applications of this instrument and this analysis technique include the development of monitoring and short-term prediction (nowcasting) of supercooled cloud liquid water, which is hazardous condition for air- and surface-transportation, as well as a weather modification opportunity.

Acknowledgements: Radiometer observations for the snow storm on 14 February 2008 are part of the dataset continually collected at Radiometrics Corporation headquarters. Radiometer and radar observations for the snow storm on 23 February 2006 are part of the dataset collected for the Canadian CloudSat Calipso Validation Project (C3VP), at Environment Canada. We wish to thank Mr. Peter Rodriguez (from Environment Canada) for maintaining the C3VP database and making it available to us. We are indebted to Prof. Frédéric Fabry (from McGill University) for providing us with displays of the X-band radar data during the C3VP field campaigns. We are also grateful to Dr. William Brown (from NCAR-EOL) for providing an early version of Figure 4. We express thanks to Dr. Alexei Korolev and Dr. Ismail Gultepe (from Environment Canada) for reviewing this manuscript before its journal submission.

REFERENCES

- Bergeron, T., 1935: On the physics of cloud and precipitation. *Proceedings of the 5th UGGI Assembly*, International Union of Geodesy and Geophysics, Lisbon, **Vol.2**, 156–178.
- Cimini, D., T. Hewison, and L. Martin, 2006a: Comparison of brightness temperatures observed from ground-based microwave radiometers during TUC. *Meteorologische Zeitschrift*, **Vol.15**, 19-25, doi: 10.1127/0941-2948/2006/0096.

- Cimini, D., T. Hewison, L. Martin, J. Gueldner, C. Gaffard, F. Marzano, 2006b: Temperature and humidity profile retrievals from ground-based microwave radiometers during TUC. *Meteorologische Zeitschrift*, **Vol.15**, 45-56, doi: 10.1127/0941-2948/2006/0099.
- Cober, S., G. Isaac, and W. Strapp, 2001: Characterizations of Aircraft Icing Environments that Include Supercooled Large Drops. *Journal of Applied Meteorology*, **Vol.40**, 1984-2002.
- Dunn, L., 1987: Cold Air Damming by the Front Range of the Colorado Rockies and its Relationship to Locally Heavy Snows. *Weather and Forecasting*, **Vol.2**, 177-189.
- Findeisen, W., 1938: Die kolloidmeteorologischen Vorgänge bei Neiderschlagsbildung (Colloidal meteorological processes in the formation of precipitation). *Meteorologische Zeitschrift*, **Vol.55**, 121–133.
- Gultepe, I., S. Cober, G. Pearson, J. Milbrandt, B. Hansen, S. Platnick, P. Taylor, M. Gordon, and J. Oakley, 2008: The Fog Remote Sensing and Modeling, (FRAM) Field Project and Preliminary Results. *Bulletin of the American Meteorological Society*, in print.
- Gunn, R., and G. Kinzer, 1949: The terminal velocity of fall for water drops in stagnant air. *Journal of Meteorology*, **Vol.15**, 243-248.
- Güldner, J., and D. Spänkuch, 2001: Remote sensing of the thermodynamic state of the atmospheric boundary layer by ground-based microwave radiometry. *Journal of Atmospheric and Oceanic Technology*, **Vol.18**, 925-933.
- Knupp, K., R. Ware, D. Cimini, F. Vandenberghe, J. Vivekanandan, E. Westwater, and T. Coleman, 2008: Ground-Based Passive Microwave Profiling during Dynamic Weather Conditions. *Journal of Atmospheric and Oceanic Technology* (submitted).
- Koldaev, A., T. Low, and W. Strapp, 1999: Microwave Measurements of Cloud Liquid Water Path and Average In-cloud Temperature at King City, Ontario, Winter 96/97. *Transport Canada Report*, **TP14104**, 94 pp.
- Korolev, A., 2007: Limitations of the Wegener–Bergeron–Findeisen Mechanism in the Evolution of Mixed-Phase Clouds. *Journal of the Atmospheric Sciences*. **Vol.64**, 3372-3375.
- Korolev, A., G. Isaac, W. Strapp, S. Cober, and H. Barker, 2007: In situ measurements of liquid water content profiles in midlatitude stratiform clouds. *Quarterly Journal of the Royal Meteorological Society*. **Vol.133**, 1693-1699, doi: 10.1002/qj.147.
- Liljegren, J., E. Clothiaux, S. Kato, and B. Lesht, 2001: Initial Evaluation of Profiles of Temperature, Water Vapor and Cloud Liquid Water from a New Microwave Profiling Radiometer. *Proceedings of the 5th Symposium on Integrated Observing Systems*, Albuquerque (NM, USA), American Meteorological Society.
- Liu, A., and W. Moore, 2004: Lake-Effect Snowstorms over Southern Ontario, Canada, and Their Associated Synoptic-Scale Environment. *Monthly Weather Review*, **Vol.132**, 2595-2609.
- Mahoney, J., J. Brown, and E. Tollerud, 1995: Contrasting Meteorological Conditions Associated with Winter Storms at Denver and Colorado Springs. *Weather and Forecasting*, **Vol.10**, 246-260.
- Parsons, D., and 12 Coauthors, 1994: The integrated sounding system: Description and preliminary observations from TOGA COARE. *Bulletin of the American Meteorological Society*, **Vol.75**, 553–567.

- Pruppacher, H., and J. Klett, 1997: *Microphysics of Clouds and Precipitation*, 2nd rev. and enl. ed. Kluwer Academic Publishers, The Netherlands.
- Radiometrics, 2007: Profiler Operator's Manual, MP-3000A, MP-2500A, MP-1500A, MP-183A. Radiometrics Corporation, Boulder, CO, USA. 87 pp.
- Rogers, R., and M. Yau, 1991: *A Short Course in Cloud Physics*, 3rd ed. Pergamon Press, England.
- Rosenkranz, P.W., 1998: Water Vapor Microwave Continuum Absorption: A Comparison of Measurements and Models. *Radio Science*, **Vol.33**, 919-928.
- Röttger, J., and M. Larsen, 1990: UHF/VHF Radar Techniques for Atmospheric Research and Wind Profiler Applications, in *Radar in Meteorology*, edited by David Atlas, pp. 235-281, American Meteorological Society, Boston, MA, USA.
- Solheim, F., J. Godwin, E. Westwater, Y. Han, S. Keihm, K. Marsh, and R. Ware, 1998: Radiometric profiling of temperature, water vapor and cloud liquid water using various inversion methods. *Radio Science*, **Vol.33**, 393-404.
- Ware, R., R. Carpenter, J. Güldner, J. Liljegren, T. Nehr Korn, F. Solheim, and F. Vandenberghe, 2003: A multi-channel radiometric profiler of temperature, humidity and cloud liquid. *Radio Science*, **Vol.38**, 8079-8032.
- Wegener, A., 1911: *Thermodynamik der Atmosphäre*. Barth, Leipzig, 331 pp.
- Zawadzki, I., F. Fabry, and W. Szyrmer, 2001: Observations of supercooled water and secondary ice generation by a vertically pointing X-band Doppler radar. *Atmospheric Research*, **Vol.59-60**, 343-359.

TABLE 1. Parameters of vertically-pointing radars

	X-band McGill VPRD	UHF-band NCAR ISS
Wavelength (frequency)	3.2 cm (9.35 GHz)	32.8 cm (915 MHz)
Pulse length	150 m	100 m and 400 m
Beam width (one way)	2°	9°
Peak transmitted power	25 kW	500 W
Pulse-repetition period	769 μ s	50 μ s and 100 μ s

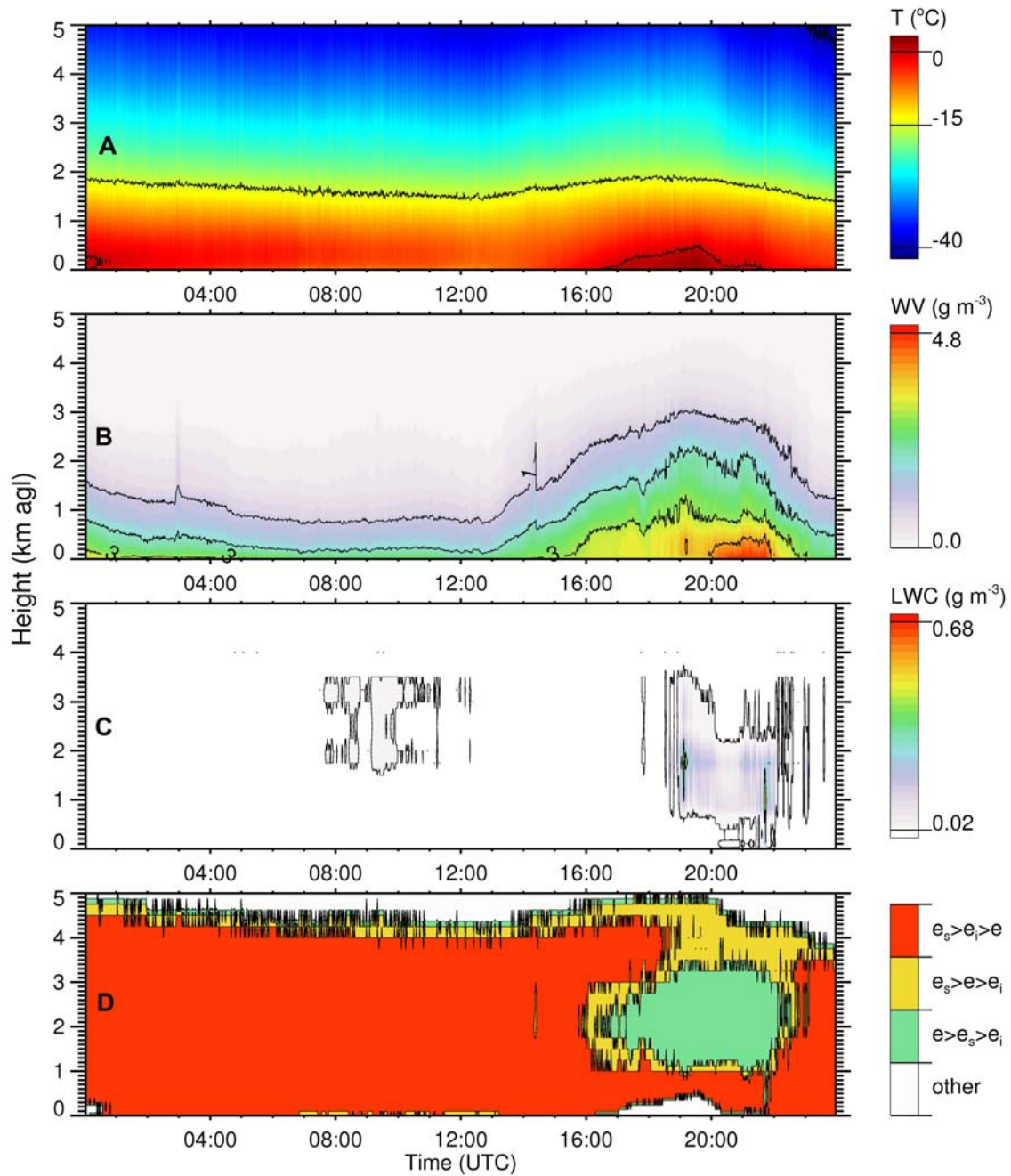


Fig. 1. Microwave profiling radiometer observations of a winter lake-effect snowstorm (North-American Great Lakes), on 23 Feb 2006 at 80 km north of Toronto, Ontario (Canada). Panels from top to bottom correspond to time-height cross sections of air temperature (in Celsius), vapor density (in g m^{-3}), cloud liquid-water content (in g m^{-3}), and vapor-pressure class, all according to the color scales on the corresponding right. The Y axes give the height in km above the ground, and the X axes correspond to the UTC time.

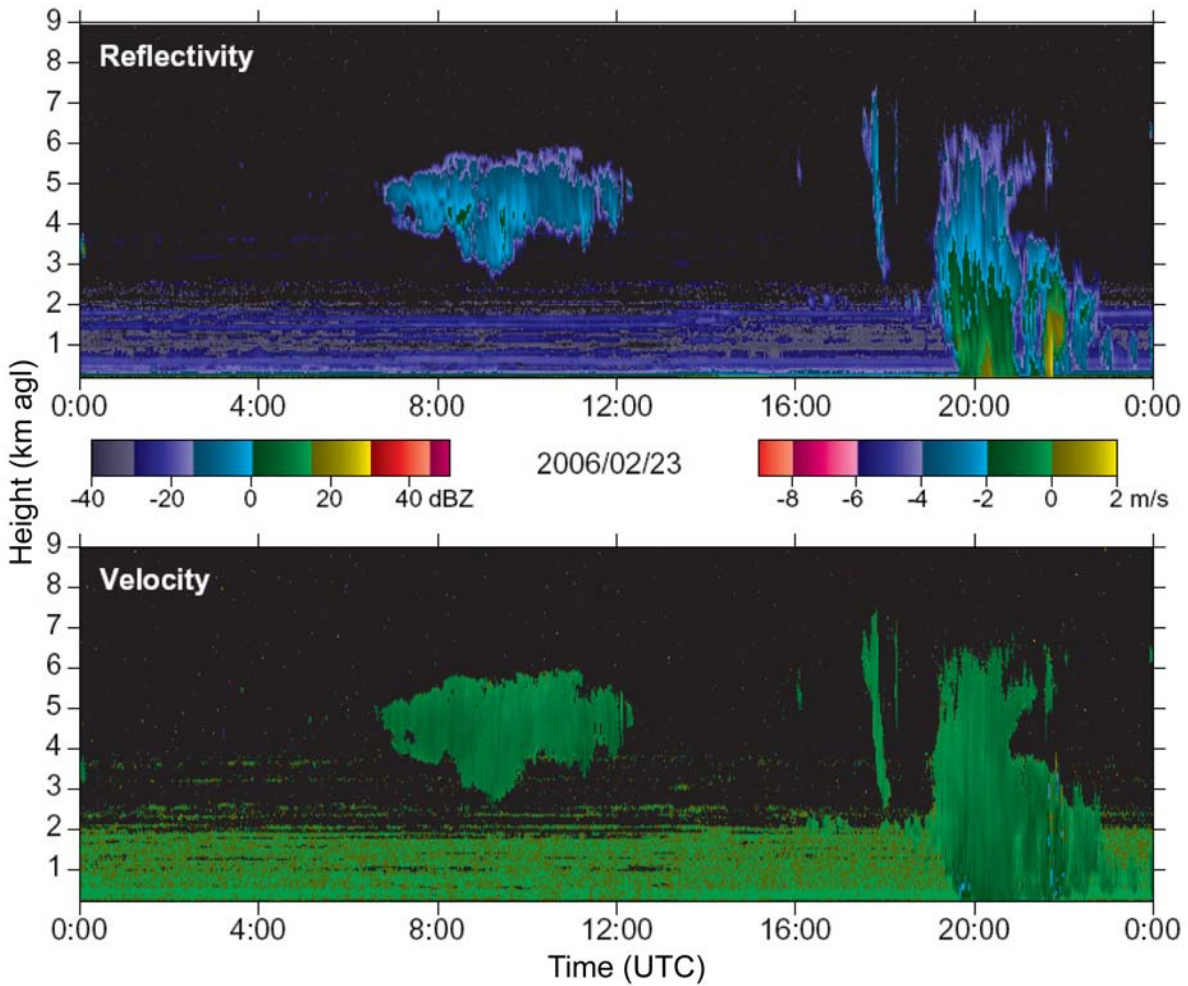


Fig. 2. X-band vertically-pointing radar observations of a winter lake-effect snowstorm (North-American Great Lakes), on 23 Feb 2006 at 80 km north of Toronto, Ontario (Canada). The upper panel correspond to time-height cross sections of radar reflectivity factor (in dBZ, according to the color scale in the left center), and the lower panel to time-height cross sections of vertical Doppler velocity (in m s^{-1} , negative downwards, according to the color scale in the right center). In both cases, the Y axis corresponds to height in km above the ground level, and the X axis to UTC time. Image courtesy of Prof. Frédéric Fabry (McGill University, Marshall Radar Observatory).

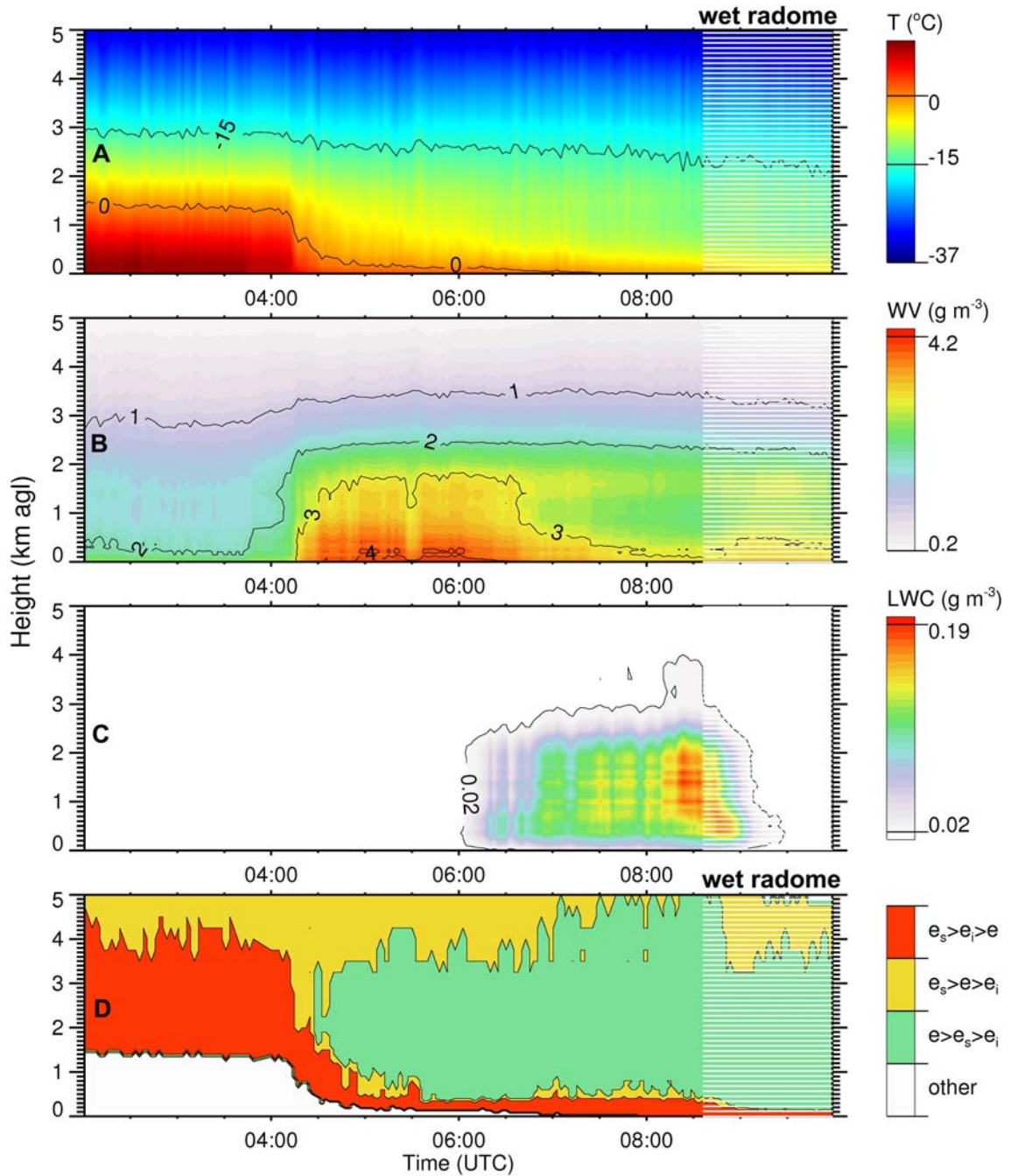


Fig. 3. Microwave profiling radiometer observations of a winter upslope snowstorm (North-American Central High Plains) at Boulder Colorado (USA) on 14 Feb 2008. Panels from top to bottom correspond to time-height cross sections of air temperature (in Celsius), vapor density (in g m^{-3}), cloud liquid-water content (in g m^{-3}), and vapor-pressure class, all according to the color scales on the right. The Y axis corresponds to height in km above the ground, and the X axis corresponds to UTC time.

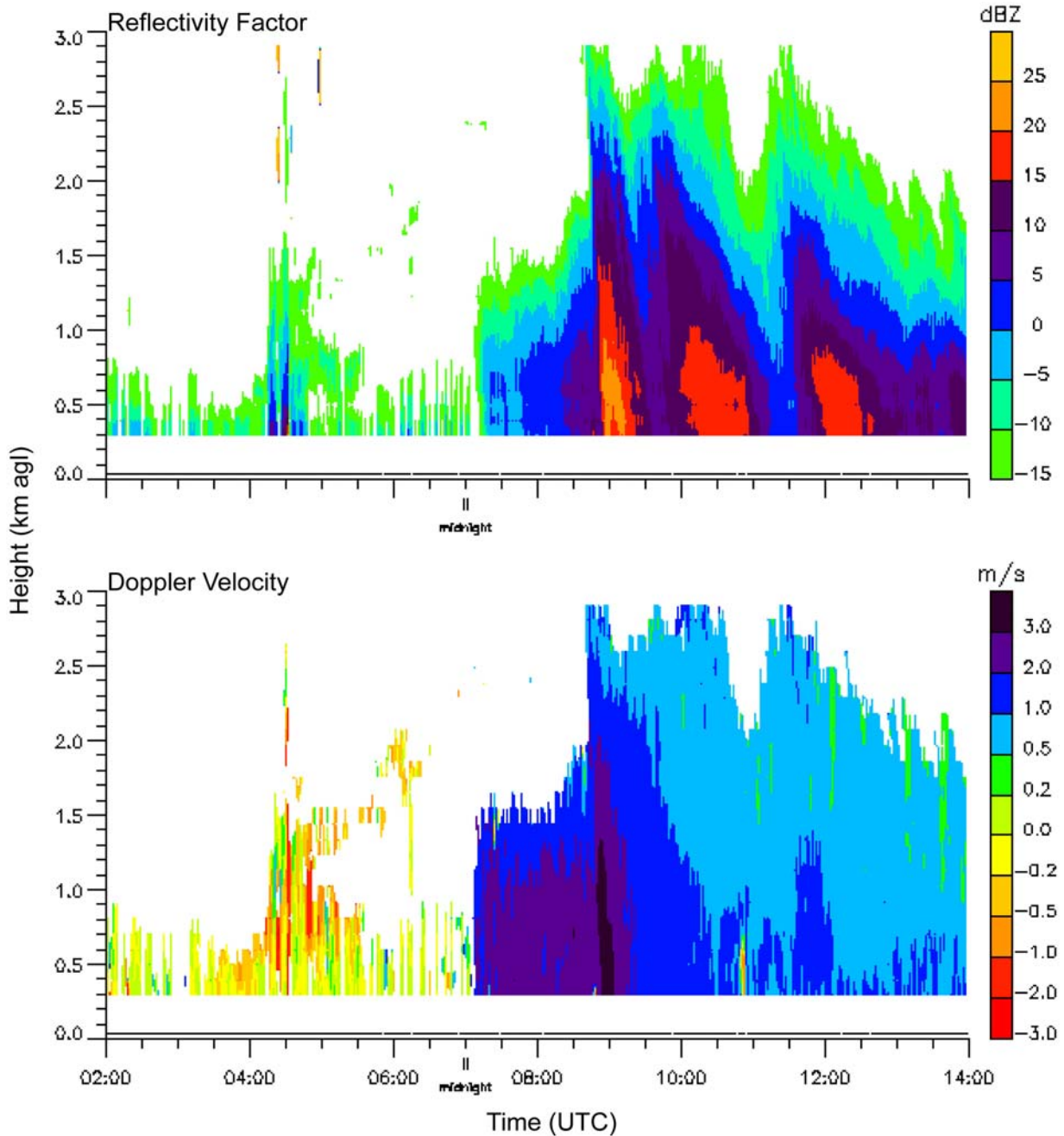


Fig. 4. UHF-band vertically-pointing radar observations of a winter upslope snowstorm (North-American Central High Plains) at Boulder Colorado (USA) on 14 Feb 2008. The upper panel correspond to a time-height cross section of radar reflectivity factor (in dBZ), and the lower panel to a time-height cross section of vertical Doppler velocity (in m s^{-1} , positive downwards), both according to the color scale on the right. The Y-axis corresponds to height in km above the ground level, and the Y axis to UTC time. Image courtesy of Dr. William Brown (NCAR, Earth Observing Laboratory).